

Long-term excitation energy transfer predicted by a modified convolutional neural networks in the FMO complexes

Yi-Meng Huang,¹ Zi-Ran Zhao,^{1,*} and Shun-Cai Zhao^{1,†}

¹*Center for Quantum Materials and Computational Condensed Matter Physics,
Faculty of Science, Kunming University of Science and Technology, Kunming, 650500, PR China*

(Dated: 00:23, Friday 25th April, 2025)

In machine learning (ML), the risk of recursive strategies overfitting historical data has driven the development of convolutional neural networks (CNNs) in simulating quantum dissipative dynamics. In this work, we propose an efficient CNNs scheme incorporating novel redundant time-functions to predict 100 picosecond (ps) excitation energy transfer (EET) in Fenna-Matthews-Olson (FMO) complexes, in which the original time t is normalized by mapping it to the $[0, 1]$ range, allowing different functions focus on distinct time intervals, thereby effectively capturing the multi-timescale characteristics of EET dynamics. This method simplifies optimization and enhances learning efficiency, and demonstrate the accuracy, robustness, and efficiency of our approach in predicting quantum dissipative dynamics.

INTRODUCTION

The nearly 100% photosynthetic conversion efficiency observed in photosynthetic organisms, such as the Fenna-Matthews-Olson (FMO) complex, has sparked considerable research interest[1–3]. This remarkable efficiency is a key prerequisite for the development of artificial photosynthetic devices[4–6]. Understanding and simulating the excitation energy transfer (EET) dynamics in the FMO complex is essential for unraveling the physics behind its remarkable efficiency. EET dynamics are typically described within the framework of open system theory, which is governed by the Hamiltonian evolution of the total system and characterized by the reduced density operator[2, 3, 7]. Several numerically exact methods have been developed to simulate the reduced dynamics, including the hierarchy of equations of motion (HEOM) technique[8], path-integral Monte Carlo[9], multi-configurational time-dependent Hartree (MCTDH)[10], the stochastic Liouville-von Neumann equation[11], time-evolving density matrix using orthogonal polynomials algorithm (TEDOPA)[12], etc. However, modeling the influence of the environment on quantum systems presents significant challenges due to the vast number of environmental degrees of freedom[13], limiting their practicality for investigating long-term quantum dynamical phenomena.

In recent years, machine learning (ML) has emerged as a powerful tool for simulating quantum dissipative dynamics[14–20]. Among these approaches, recursive ML strategies[21–26] predict future dynamics based on historical data[27–30], resembling traditional quantum dynamics where the system’s evolution explicitly depends on its current state and implicitly on prior states. However, these recursive methods often suffer from overfitting to past data, as well as from issues like gradient disappearance or explosion, which may violate fundamental physical principles such as trace conservation of the density matrix. To address these challenges, convolutional neural networks (CNNs)[17, 29] have been proposed as a more effective approach for predicting quantum dynamical evolution, aiming to overcome the limitations of recursive methods and better preserve the system’s physical constraints.

In this work, we adopt a refined spatiotemporal mapping approach with the Quantum Toolbox in Python (QuTiP)[31] in combination with CNNs. After collecting EET dynamics data from the FMO complex through numerical simulations, we endow the data with specific physical connotations by integrating the evolution of time with the physical laws governing EET dynamics, where time redundant-functions are explicitly reflected. Consequently, time points that were previously unrelated to physical systems are now incorporated as features in the

CNNs.

Consequently, time points that were previously unrelated to physical systems are now incorporated as features in our CNN-based approach. Additionally, the intrinsic correlations between chlorophyll sites in the FMO complex are incorporated into the label construction, providing the neural network with a solid physical foundation in this work. This refined spatiotemporal mapping allows the model to make accurate predictions in both temporal (from 0 to 100 ps) and environmental extrapolations (using environmental parameters outside the training set). As a result, the model's stability and performance are significantly enhanced, effectively preventing issues such as gradient disappearance and explosion that typically arise in long-term numerical simulations.

THEORETICAL MODEL

Quantum dynamics of the FMO complex

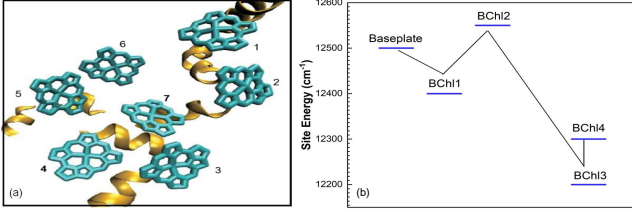


FIG. 1. (a) Seven bacteriochlorophyll (BChl) molecules in the FMO pigment-protein complex. (b) The energy transfer pathways in the FMO complex: baseplate \rightarrow BChls 1 \rightarrow 2 \rightarrow 3 \rightarrow 4 with the initial excitation BChl 1.

The energy flow within the FMO complex has been shown to primarily occur through two main excitation energy transfer (EET) pathways[32]. These pathways link bacteriochlorophylls (BChls) that are spatially close and excitonically coupled, as demonstrated by Brixner et al. leveraging a two-dimensional electronic spectroscopy[33]. In the subsequent analysis, we will examine the quantum dynamics of EET based on the energy flow pathways depicted in Fig.1(b). The Hamiltonian governing this process comprises three components: the electronic state Hamiltonian \hat{H}_e , the environmental phonon Hamiltonian \hat{H}_{ph} , and the electron-phonon interaction Hamiltonian

\hat{H}_{el-ph} [34], as follows:

$$\hat{H}_t = \hat{H}_e + \hat{H}_{ph} + \hat{H}_{el-ph}, \quad (1)$$

$$\hat{H}_e = \sum_{j=1}^7 \epsilon_j |j\rangle \langle j| + \sum_{h=1, h \neq j}^7 J_{jh} |j\rangle \langle h|, \quad (2)$$

$$\hat{H}_{ph} = \sum_{\xi} \hbar \omega_{\xi} \hat{b}_{\xi}^{\dagger} \hat{b}_{\xi}, \quad (3)$$

$$\hat{H}_{el-ph} = \sum_{j=1}^7 (\lambda_j + \hat{u}_j) |j\rangle \langle j|, \quad (4)$$

$$\hat{u}_j = - \sum_{\xi} c_{j\xi} \hat{q}_{\xi}. \quad (5)$$

Each pigment is modeled as a two-level system, where $|j\rangle$ denotes the excited state of the j -th pigment molecule. Here, ϵ_j represents the site energy of the j -th pigment molecule in Eq.(2), and J_{jk} describes the electronic coupling strength between the j -th and k -th pigment molecules.

In the expression for \hat{H}_{ph} given by Eq.(3), ω_{ξ} is the frequency of the ξ -th phonon mode, while \hat{b}_{ξ}^{\dagger} and \hat{b}_{ξ} are the creation and annihilation operators of the ξ phonon mode, respectively. In Eq.(4), λ_j represents the reorganization energy at site j , modeled using the continuous Drude-Lorentz spectral density as described in Eq.(6).

$$J_j(\omega) = 2\lambda_j \frac{\omega \gamma_j}{\omega^2 + \gamma_j^2} \quad (6)$$

Considering the influence of discrete molecular modes on population dynamics[35], $c_{j\xi}$ in Eq.(5) represents the coupling constant between the j -th pigment molecule and the ξ -th phonon mode, while \hat{q}_{ξ} denotes the dimensionless coordinate of the ξ -th phonon mode. The reference quantum dynamics trajectories for the reduced density matrix of the system are propagated using the local thermalizing Lindblad master equation[36]. The Adolphs and Renger Hamiltonian, describing seven sites per subunit[37], is employed as follows:

$$\begin{bmatrix} 200 & -87.7 & 5.5 & -5.9 & 6.7 & -13.7 & -9.9 \\ -87.7 & 320 & 30.8 & 8.2 & 0.7 & 11.8 & 4.3 \\ 5.5 & 30.8 & 0 & -53.5 & -2.2 & -9.6 & 6.0 \\ -5.9 & 8.2 & -53.5 & 110 & -70.7 & -17.0 & -63.3 \\ 6.7 & 0.7 & -2.2 & -70.7 & 270 & 81.1 & -1.3 \\ -13.7 & 11.8 & -9.6 & -17.0 & 81.1 & 420 & 39.7 \\ -9.9 & 4.3 & 6.0 & -63.3 & -1.3 & 39.7 & 230 \end{bmatrix}$$

The energies are given in cm^{-1} , with each site interacting independently with its surrounding environment, which is characterized by the Drude-Lorentz spectral density as described in Eq. (6).

Novle redundant time-functions

Accurately capturing time-dependent dynamics, such as the evolution of density matrices in quantum transport systems, is crucial for understanding molecular excited states. However, directly inputting raw time variables into neural networks can introduce several challenges: the presence of vast time scales, localized sensitivity in temporal resolution (which may lead to overfitting in certain intervals while underfitting others), and difficulties in handling infinite-time limits, such as steady states or relaxation endpoints.

To address these challenges, the concept of redundant time-functions has been incorporated into neural networks [17] to encode temporal information, thereby enhancing the model's robustness and expressiveness in describing time-dependent processes. Specifically, each logistic function is spaced by t ps apart and covers a local time window t . Collectively, the 100 logistic functions span from negative time to approximately $100t$ ps, enhancing the time resolution. This distributed temporal encoding, achieved through overlapping logistic functions, ensures that each time point is covered by multiple functions, akin to a sliding time window, thereby eliminating reliance on single-point inputs and improving multi-scale feature extraction. Inspired by this approach [17], we propose a refined redundant time-function, defined as:

$$f_k(t_n) = \frac{\eta_k(t_n) + g_k(t_n)}{14}, \quad (7)$$

$$\eta_k(t_n) = \tanh\left(\frac{t_n}{4} + \frac{k}{35}\right), \quad (8)$$

$$g_k(t_n) = \frac{13}{1 + 15 \exp[-0.02(40t_n + 4k - 1)]}. \quad (9)$$

The logistic function $f_k(t_n)$ exhibits smooth S-shaped characteristics, allowing the original time t to be mapped onto the $[0, 1]$ range, thereby normalizing the time input. To improve prediction accuracy, we incorporated

the \tanh function (Eq.(8)) in addition to modifying the logistic function (Eq.(9)).

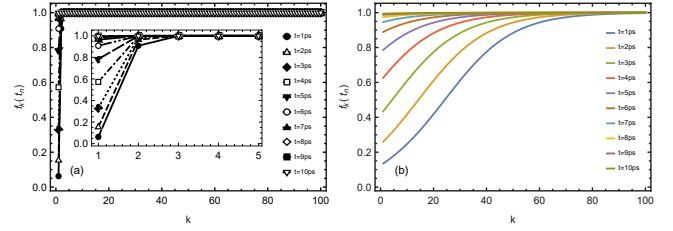


FIG. 2. Evolutions of redundant time-functions $f_k(t_n)$ with respect to parameter k at different moments, $k \in \{0, 1, 2, \dots, 99\}$. (a) Redundant time-functions in Ref.[17] with an inset displaying for $k \in [0, 5]$. (b) Novel redundant time-functions.

As shown in Ref.[17], the redundant time-functions achieve normalization only when $k \geq 3$ (as illustrated in Fig. (2)(a)). In contrast, the functions proposed in this work (Fig. 2(b)) exhibit significantly enhanced robustness and superior performance in long-term predictions. These functions achieve normalization across distinct time intervals, including early-stage rapid evolution, mid-stage transitions, and long-term steady states, thereby effectively capturing the multi-timescale characteristics of quantum dynamics. Moreover, even in the presence of parameter fluctuations or noise, the redundancy introduced through numerous overlapping logistic functions ensures that alternative functions remain effective in providing temporal information. This design enhances fault tolerance, guaranteeing the complete encoding of the dynamical process from transient behavior to steady state, thereby preventing information loss and ensuring full-time coverage. Consequently, these refined redundant time-functions serve as critical input features for convolutional neural networks (CNNs), enabling them to efficiently learn complex dynamical laws and accurately predict the long-term evolution of quantum system configurations.

Data architecture of CNN

In this study, key physical parameters governing excitation energy transfer (EET) were selected as features for the convolutional neural network (CNN). The reorganization energy

(Energy level)/10	γ_a	λ_b	T_c	$\{f_k(t_m)\}$	$\{\rho_{ii}(t_m)\}$	$\sum_{i=1}^6 \text{Abs}(\rho_{ii} - \rho_{i+1,i+1})$	$\sum_{i=1}^7 \rho_{ii}(t_j)$
0.1	γ_1	λ_1	T_1	$f_k(t_0)$	$\rho_{11}(t_0)$	$\text{Abs}(\rho_{11}(t_0) - \rho_{22}(t_0))...$	$\rho_{11}(t_0) + \rho_{22}(t_0)...$
\vdots	\vdots	\vdots	\vdots	\vdots	\vdots	\vdots	\vdots
0.1	γ_1	λ_1	T_1	$f_k(t_m)$	$\rho_{11}(t_m)$	$\text{Abs}(\rho_{11}(t_m) - \rho_{22}(t_m))...$	$\rho_{11}(t_m) + \rho_{22}(t_m)...$
0.1	γ_2	λ_1	T_1	$f_k(t_0)$	$\rho_{11}(t_0)$	$\text{Abs}(\rho_{11}(t_0) - \rho_{22}(t_0))...$	$\rho_{11}(t_0) + \rho_{22}(t_0)...$
\vdots	\vdots	\vdots	\vdots	\vdots	\vdots	\vdots	\vdots
0.1	γ_2	λ_1	T_1	$f_k(t_m)$	$\rho_{11}(t_m)$	$\text{Abs}(\rho_{11}(t_m) - \rho_{22}(t_m))...$	$\rho_{11}(t_m) + \rho_{22}(t_m)...$
\vdots	\vdots	\vdots	\vdots	\vdots	\vdots	\vdots	\vdots
0.1	γ_m	λ_1	T_1	$f_k(t_m)$	$\rho_{11}(t_m)$	$\text{Abs}(\rho_{11}(t_m) - \rho_{22}(t_m))...$	$\rho_{11}(t_m) + \rho_{22}(t_m)...$
0.1	γ_1	λ_2	T_1	$f_k(t_0)$	$\rho_{11}(t_0)$	$\text{Abs}(\rho_{11}(t_0) - \rho_{22}(t_0))...$	$\rho_{11}(t_0) + \rho_{22}(t_0)...$
\vdots	\vdots	\vdots	\vdots	\vdots	\vdots	\vdots	\vdots
0.1	γ_1	λ_j	T_1	$f_k(t_m)$	$\rho_{11}(t_m)$	$\text{Abs}(\rho_{11}(t_m) - \rho_{22}(t_m))...$	$\rho_{11}(t_m) + \rho_{22}(t_m)...$
0.1	γ_1	λ_1	T_2	$f_k(t_0)$	$\rho_{11}(t_0)$	$\text{Abs}(\rho_{11}(t_0) - \rho_{22}(t_0))...$	$\rho_{11}(t_0) + \rho_{22}(t_0)...$
\vdots	\vdots	\vdots	\vdots	\vdots	\vdots	\vdots	\vdots
0.1	γ_1	λ_1	T_j	$f_k(t_m)$	$\rho_{11}(t_m)$	$\text{Abs}(\rho_{11}(t_m) - \rho_{22}(t_m))...$	$\rho_{11}(t_m) + \rho_{22}(t_m)...$
Features				Labels			

TABLE I. Parameters used in the training structure for convolutional neural network (CNN) architecture: labels for chlorophyll sites were divided by 10, i.e., the input elements corresponding to the columns in the reduced density matrix are $\{0.1, 0.2, 0.3, \dots, 0.7\}$. Time-functions based on the logistic were defined as $f_k(t_n) = \frac{\eta_k(t_n) + g_k(t_n)}{14}$, $\eta_k(t_n) = \tanh(\frac{t_n}{4} + \frac{k}{35})$, $g_k(t_n) = \frac{13}{1 + 15 \exp[-0.02(40t_n + 4k - 1)]}$, $t_n = \{t_0, t_1, \dots, t_m\}$, $k \in \{0, 1, 2, \dots, 99\}$, $\gamma_a = \{\gamma_0, \gamma_1, \dots, \gamma_j\}$, $\lambda_b = \{\lambda_0, \lambda_1, \dots, \lambda_j\}$, $T_c = \{T_0, T_1, \dots, T_j\}$.

(λ) characterizes the coupling strength between molecules and their environment, directly influencing energy transfer efficiency. The characteristic frequency (γ) describes the bath relaxation rate, reflecting the environment's response speed to excited-state evolution. Temperature (T) impacts thermal fluctuations and decoherence processes, thereby altering the quantum energy transfer efficiency. Additionally, the novel redundant time-functions were incorporated to normalize the temporal domain, facilitating the network's capacity to capture both short-term quantum beats and long-term asymptotic behavior. As presented in Tab. I, all relevant parameters are explicitly outlined in the Features column.

The learning objectives of the CNN, corresponding to the predicted outputs, serve as labels to represent the dynamical evolution of the FMO system. In contrast to Ref. [17], where only the diagonal elements $\rho_{jj}(t)$ were employed to represent exciton populations at each BChl site and track EET, this work expands the learning targets by introducing two additional labels: $\sum_{i=1}^6 |\rho_{ii} - \rho_{i+1,i+1}|$ and $\sum_{i=1}^7 \rho_{ii}(t_j)$. The term

$\sum_{i=1}^6 |\rho_{ii} - \rho_{i+1,i+1}|$ tracks fluctuations in population dynamics between adjacent energy states, improving the model's sensitivity to population imbalances and enhancing its ability to predict transitions in energy transfer processes. These complementary labels enhance the model's predictive accuracy, providing a more comprehensive description of EET dynamics. The aforementioned label data are clearly indicated in the labels column of Tab. I.

To prepare the dataset, several preprocessing steps were applied to ensure effective model training. The labels associated with the seven sites were scaled down by a factor of 10, resulting in normalized values ranging from 0.1 to 0.7. Additionally, λ was divided by 100, while γ and T were each divided by 1000 to standardize their magnitudes. Temporal variables were normalized leveraging 100 redundant time-functions $f_k(t_n)$, constructed from logistic functions with k ranging from 0 to 99. This preprocessing procedure effectively scales and normalizes the input data, ensuring that the CNN can accurately learn the underlying physical processes governing EET.

RESULTS AND DISCUSSIONS

Training model validation

To ensure the reliability of the CNN model, we validated it using a dataset spanning 7 picoseconds (ps), comprising 301 evenly distributed time points between 0 and 7 ps. The EET dynamic evolution trajectories for each site of the FMO complex were generated using the QuTiP method. These trajectories, covering the 0 to 7 ps range (denoted as $m = 7$), were simulated under varying environmental parameters: reorganization energy (λ) ranging from 14 to 28 cm^{-1} , characteristic frequency (γ) from 150 to 164 cm^{-1} , and temperature (T) from 270 to 284 K. Each environmental parameter was assigned 15 distinct values within its respective range. Based on this setup, the number of rows in Table I is determined by Eq. (10), the number of feature columns is calculated using Eq. (11), and the j -th label column is derived from Eq. (12).

$$N_{\text{rows}} = n_{\text{Energysites}} \times n_{\text{Timepoints}} \times n_{\gamma} \times n_{\lambda} \times n_T, \quad (10)$$

$$N_{\text{Features}} = n_{\text{Energysites}} + n_{\gamma} + n_{\lambda} + n_T + n_{f_k(t_m)}, \quad (11)$$

$$\text{Labels}_j = \text{Energysite}_j + \sum_{i=1}^6 [|\rho_{jj} - \rho_{i+1,i+1}| + (\rho_{jj} + \rho_{i+1,i+1})] \quad (12)$$

In Eq.(10)~(11), n represents the number of corresponding parameter, and the subscript j denotes the j -th site in Eq.(12). Following this procedure, a feature matrix with dimensions $7, 111, 125 \times 104$ is constructed, accompanied by a label matrix of dimensions $7, 111, 125 \times 13$. Transforming the dataset into this matrix format enables the CNN to efficiently process the data while maintaining high predictive accuracy, making it a suitable choice for training and prediction.

In the resulting matrix, the first column corresponds to the population value of the current energy level at a given time. Columns 2~7 contain the absolute values of the population differences between the current energy level and the others at that same time, while columns 8~13 represent the sums of the populations of the current energy level and the others at that moment. Subsequently, the convolutional output matrix is compared with the label matrix to compute the loss, for which the mean squared error (MSE) is adopted in this study. Through iterative backpropagation and continuous optimization, the final CNN model is obtained (Codes-for-CNN).

In Fig. 3, the CNN model incorporating the refined redundant time-functions was validated for predicting the evolution of the seven-site configuration over a 7 ps timescale. Under the given environmental parameters ($\lambda = 15 \text{ cm}^{-1}$, $\gamma = 175 \text{ cm}^{-1}$, and $T = 155 \text{ K}$), the green solid lines (theoretical values) and the black dashed lines (CNN-predicted values) exhibit near-complete overlap, indicating a strong agreement between the theoretical calculations and the model's predictions.

In recent studies such as Ref.[21, 38], recursive methods have been employed to predict quantum dynamics, where each step's prediction depends on the outcome of the previous one. However, these methods are often susceptible to error accumulation over time, which compromises long-term prediction accuracy. In contrast, the approach presented in this work introduces a non-recursive convolutional neural network (CNN) architecture that directly predicts the excitation energy transfer (EET) dynamics over the entire temporal domain, without relying on the previous step's result. This architecture not only prevents error propagation but also reduces computational costs, making it more efficient and accurate, especially when applied to long-term predictions over 100 ps. Furthermore, the incorporation of refined redundant time-functions provides a more robust temporal encoding, enabling the model to capture the multi-timescale nature of quantum dynamics. These innovations make our approach a significant improvement over previous methods that struggled with long-term stability and computational efficiency.

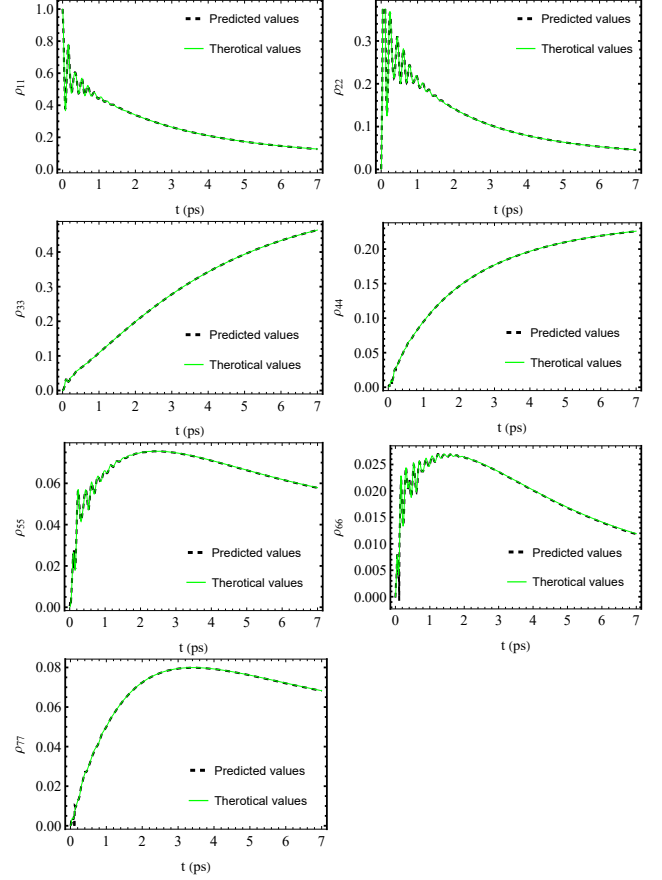


FIG. 3. Population dynamics of the seven chlorophyll sites with green solid lines being theoretical values and black dashed lines being predicted values in the FMO complex within 7 ps. Other parameters are $\lambda=15 \text{ cm}^{-1}$, $\gamma=275 \text{ cm}^{-1}$, $T=155 \text{ K}$.

Long-term prediction of EET

The CNN model incorporating redundant time-functions, as shown in Fig. 3, effectively captures the detailed evolution of the seven-site configuration over a 7-picosecond timescale. Building on the refined redundant time-functions and the distinct labels introduced in this work, we further explored the system's dynamical behavior over longer timescales. To achieve this, data from the 0~7 ps period were collected using the QuTiP tool, serving as the training set for predicting the dynamical evolution of the FMO complex over the 0~100 ps timeframe. The environmental parameters for training were set as follows: λ : $28\sim30 \text{ cm}^{-1}$, γ : $164\sim170 \text{ cm}^{-1}$, T : $284\sim290 \text{ K}$.

In Fig. 4, the population predictions for each chlorophyll site are extended to 100 ps, with both the predicted results and theoretical calculations plotted on the same graph for di-

rect comparison. To better illustrate the population dynamics over an extended timescale, logarithmic scales are applied to the insets of each panel. The green solid lines, representing theoretical values, and the black dotted lines, denoting predicted results, exhibit remarkable agreement over the 100-ps period. Notably, around the 10-ps mark, the population dynamics of the FMO system show a tendency toward stabilization, consistent with the findings reported in Ref. [17]. The incorporation of modified redundant time-functions in this work significantly extends the prediction timeframe, offering a more comprehensive perspective on the long-term population evolution.

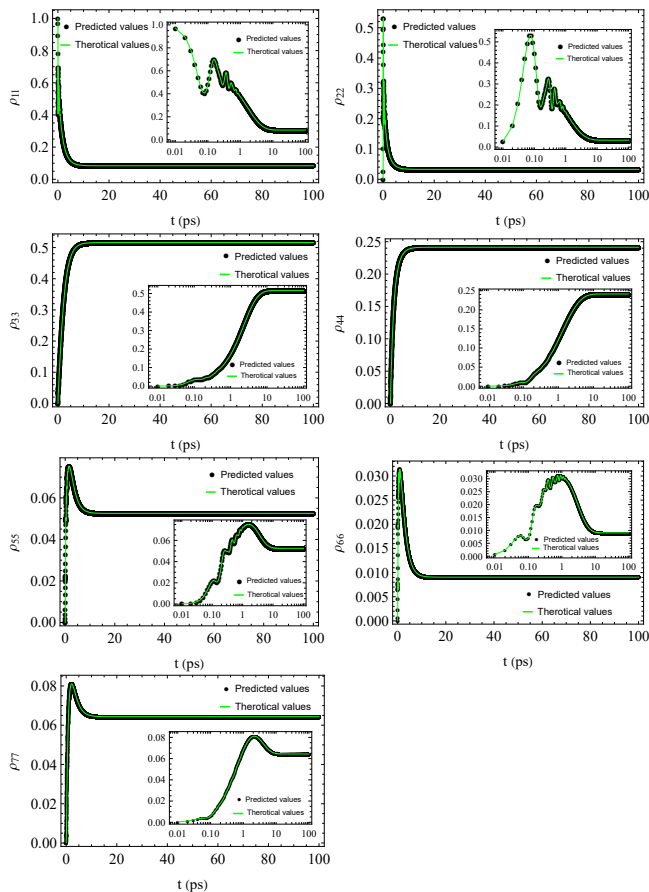


FIG. 4. Population dynamics of the seven chlorophyll sites with green solid lines being theoretical values and black dotted lines being predicted values in the FMO complex within 100 ps. The inset plots are in logarithmic scale. Other parameters are $\lambda=30 \text{ cm}^{-1}$, $\gamma=286 \text{ cm}^{-1}$, $T=166 \text{ K}$.

Compared with the 2.5-picosecond prediction reported in Ref [17], our CNN-based approach significantly outperforms previous models, including those from Ref. [21, 38], in predicting long-term excitation energy transfer (EET) dynam-

ics. For instance, while traditional redundant time-functions in Ref. [17] were limited to accurate predictions within a 2.5 ps time frame, our approach successfully extends the prediction period to 100 ps with remarkable accuracy, as shown in Fig. 4. The green solid lines (theoretical values) and black dotted lines (CNN-predicted values) exhibit near-complete overlap, demonstrating the model's high predictive accuracy even over extended timescales. The novel redundant time-functions (Eq.7) introduced in this work not only enhance the robustness of our model against parameter fluctuations but also ensure that the dynamical processes, from transient behavior to steady-state evolution, are accurately captured. This substantial improvement in prediction stability and accuracy makes our method a promising candidate for simulating long-term quantum dynamics in complex systems.

The performance improvement in this work can be attributed to several key factors. First, the CNN's exceptional feature extraction capability enables it to capture short-term dynamic features in temporal evolution by leveraging convolutional kernels to process input data, effectively identifying intrinsic correlations in energy distributions across different time points. Second, the CNN's translation invariance allows it to recognize recurring dynamic patterns regardless of their temporal position, enhancing its robustness in predicting long-term evolution. Third, the network's multi-layer architecture facilitates hierarchical feature extraction, where pooling layers reduce data dimensionality while preserving essential features, thereby improving computational efficiency and mitigating overfitting.

Moreover, the multi-timescale characteristics generated by the redundant time-functions (Eq.7) normalization across the early-stage rapid evolution, mid-stage transitions, and long-term steady states, further enhances predictive accuracy, extending the model's capability to capture long-term EET dynamics beyond the performance reported in Ref.[17]. This methodological advancement extends the model's predictive power to longer timescales, offering deeper insights into the quantum dynamics of the system. Therefore, our CNN architecture with the refined redundant time-functions offers several advantages over previous recursive methods. Not only does it reduce error propagation and computational costs, but it also enhances the model's ability to capture the multi-timescale dynamics of quantum systems. This work, therefore, provides a valuable contribution to the development of machine learning-based models for quantum dissipative systems.

CONCLUSION AND OUTLOOK

In summary, this work introduces a novel redundant time-function as a CNN input feature and uses distinct labels to predict EET dynamics across seven sites in the FMO complex, where the temporal evolution was explicitly partitioned into distinct regimes (rapid, transitional, and steady-state). These functions, combined with physically informed labels encoding population differences and sums, enable CNNs to achieve quantitative agreement with theoretical benchmarks in simulating 100 ps EET across all seven chlorophyll sites of the FMO complex. Crucially, the method eliminates error propagation inherent to recursive strategies, demonstrating robustness. This approach not only validates CNNs for long-term quantum dynamics prediction but also provides a generalizable architecture for modeling dissipative processes. By bridging machine learning with quantum physics, the framework offers a scalable pathway to optimize artificial light-harvesting systems and accurately forecasts long-term quantum system dynamics under various external conditions.

CODE AVAILABILITY

The code is available at: [Codes-for-CNN](#) and [Codes-for-all-Figs](#).

AUTHOR CONTRIBUTIONS

S. C. Zhao conceived the idea. Y. M. Huang performed the numerical computations and wrote the draft, and S. C. Zhao did the analysis and revised the paper. Z. R. Zhao participated in part of the discussion.

ACKNOWLEDGMENT

We thank the financial supports from the National Natural Science Foundation of China (Grant Nos. 62065009 and 61565008), and the General Program of Yunnan Applied Basic Research Project, China (Grant No. 2016FB009).

DATA AVAILABILITY STATEMENT

This manuscript has associated data in a data repository. [Authors' comment: All data included in this manuscript are available upon reasonable request by contacting with the corresponding author.]

CONFLICT OF INTEREST

The authors declare that they have no conflict of interest. This article does not contain any studies with human participants or animals performed by any of the authors. Informed consent was obtained from all individual participants included in the study.

* Co-first author.

† Corresponding author: zsczhao@126.com.

- [1] F. H. Alharbi and S. Kais. Theoretical limits of photovoltaics efficiency and possible improvements by intuitive approaches learned from photosynthesis and quantum coherence. *Renew. and Sustain. Ener. Rev.*, 43:1073, 2014.
- [2] L. F. Li, S. C. Zhao, and L. X. Xu. Influence of the coupled-dipoles on photosynthetic performance in a photosynthetic quantum heat engine. *Chin. Phys.s B*, 30:044215, 2021.
- [3] L. F. Li, S. C. Zhao, and L. X. Xu. Charge-transport enhanced by the quantum entanglement in the photosystem ii reaction center. *Europ Phys J Plus*, 136:1–11, 2021.
- [4] S. Maity, B. M. Bold, J. D. Prajapati, M. Sokolov, T. Kubar, M. Elstner, and U. Kleinekathfer. Dftb/mm molecular dynamics simulations of the fmo light-harvesting complex. *J Phys. Chem. Lett.*, 11:8660–8667, 2020.
- [5] J. Schulze, M. F. Shibl, M. J. Al-Marri, and O. Kuhn. Multi-layer multi-configuration time-dependent hartree (ml-mctdh) approach to the correlated exciton-vibrational dynamics in the fmo complex. *J Chem. Phys.*, 144 18:185101, 2016.
- [6] I. G. Karafyllidis. Quantum transport in the fmo photosynthetic light-harvesting complex. *J. Bio. Phys.*, 43:239–45, 2017.
- [7] P. Huo and T. F. Miller. Electronic coherence and the kinetics of inter-complex energy transfer in light-harvesting systems. *Phys Chem. Chem. Phys.*, 17 46:30914–24, 2015.
- [8] Y. Tanimura. Numerically "exact" approach to open quantum dynamics: The hierarchical equations of motion (heom). *J. Chem. Phys.*, 153 2:020901, 2020.
- [9] D. Kast and J. Ankerhold. Persistence of coherent quantum dynamics at strong dissipation. *Phys. Rev. Lett.*, 110 1:010402, 2012.
- [10] Hans-Dieter Meyer, Uwe Manthe, and Lorenz S. Cederbaum. The multi-configurational time-dependent hartree approach. *Chem. Phys. Lett.*, 165:73–78, 1990.

- [11] J. T. Stockburger and H. Grabert. Exact c-number representation of non-markovian quantum dissipation. Phys. Rev. Lett., 88 17:170407, 2002.
- [12] J. Prior, A. W. Chin, S. F. Huelga, and M. B. Plenio. Efficient simulation of strong system-environment interactions. Phys. Rev. Lett., 105 5:050404, 2010.
- [13] A. J. Leggett, S. Chakravarty, A. T. Dorsey, Matthew P. A. Fisher, A. Garg, and W. Zwerger. Dynamics of the dissipative two-state system. Rev. Mod. Phys., 59:1–85, Jan 1987.
- [14] S. Hochreiter and J. Schmidhuber. Long short-term memory. Neural Computation, 9:1735–1780, 1997.
- [15] K. Lin, J. Peng, F. L. Gu, and Z. Lan. Simulation of open quantum dynamics with bootstrap-based long short-term memory recurrent neural network. J Phys. Chem. Lett., 12:10225–10234, 2021.
- [16] D. Lemm, G. F. von Rudorff, and O. A. von Lilienfeld. Machine learning based energy-free structure predictions of molecules, transition states, and solids. Nat. Comm., 12:4468, 2021.
- [17] A. Ullah and P. O. Dral. Predicting the future of excitation energy transfer in light-harvesting complex with artificial intelligence-based quantum dynamics. Nat. Comm., 13, 2022.
- [18] K. Naicker, I. Sinayskiy, and F. Petruccione. Machine learning for excitation energy transfer dynamics. Phys. Rev. Research, 4:033175, 2021.
- [19] Y. Han, I. Ali, Z. Wang, J. Cai, S. c. Wu, J. Tang, L. Zhang, J. Ren, R. Xiao, Q. Lu, L. Hang, H. Luo, and J. Li. Machine learning accelerates quantum mechanics predictions of molecular crystals. Phys. Rep., 934:1–71, 2021.
- [20] K. Lin, J. Peng, C. Xu, F. L. Gu, and Z. Lan. Automatic evolution of machine-learning-based quantum dynamics with uncertainty analysis. J. Chem. Theor. and Comput., 18:5837–5855, 2022.
- [21] Arif Ullah and Pavlo O. Dral. Speeding up quantum dissipative dynamics of open systems with kernel methods. New J. Phys., 23:113019, 2021.
- [22] Arif Ullah and Pavlo O. Dral. One-shot trajectory learning of open quantum systems dynamics. J. Phys. Chem. Lett., pages 6037–6041, 2022.
- [23] Daxin Wu, Zhubin Hu, Jiebo Li, and Xiang Sun. Forecasting nonadiabatic dynamics using hybrid convolutional neural network/long short-term memory network. J. Chem. Phys., 155 22:224104, 2021.
- [24] Alexey V. Akimov. Extending the time scales of nonadiabatic molecular dynamics via machine learning in the time domain. J. Phys. Chem. Lett., pages 12119–12128, 2021.
- [25] Luis E. Herrera Rodríguez, Arif Ullah, Kennet J Rueda Espinosa, Pavlo O. Dral, and Alexei A. Kananenka. A comparative study of different machine learning methods for dissipative quantum dynamics. Mach. Learn.: Sci. Technol., 3:045016, 2022.
- [26] Kunni Lin, Jiawei Peng, Chao Xu, Feng Long Gu, and Zhenggang Lan. Automatic evolution of machine-learning-based quantum dynamics with uncertainty analysis. J. Chem. Theory Comput., 18:5837–5855, 2022.
- [27] A. Ullah and P. O. Dral. Speeding up quantum dissipative dynamics of open systems with kernel methods. New J. Phys., 23, 2021.
- [28] L. E. Herrera Rodríguez, A. Ullah, K. J. Rueda Espinosa, P. O. Dral, and A. A. Kananenka. A comparative study of different machine learning methods for dissipative quantum dynamics. Machine Learning: Sci. and Tech., 3, 2022.
- [29] L. E. Herrera Rodríguez and A. A. Kananenka. Convolutional neural networks for long time dissipative quantum dynamics. J. Phys. Chem. Lett., pages 2476–83, 2020.
- [30] L. E. Herrera Rodríguez and A. A. Kananenka. A short trajectory is all you need: A transformer-based model for long-time dissipative quantum dynamics. J Chem. Phys., 161 17, 2024.
- [31] J. Johansson, P. D. Nation, and F. Nori. Qutip: An open-source python framework for the dynamics of open quantum systems. Comput. Phys. Commun., 183:1760–1772, 2011.
- [32] R. E. Fenna and B. W. Matthews. Chlorophyll arrangement in a bacteriochlorophyll protein from chlorobium limicola. Nature, 258:573, 1975.
- [33] T. Brixner, J. Stenger, H. M. Vaswani, M. Cho, R. E. Blankenship, and G. R. Fleming. Two-dimensional spectroscopy of electronic couplings in photosynthesis. Nature, 434:625–628, 2005.
- [34] A. Ishizaki and G. R. Fleming. Theoretical examination of quantum coherence in a photosynthetic system at physiological temperature. PNAS, 106(41):17255–17260, 2009.
- [35] P. Nalbach and M. Thorwart. The role of discrete molecular modes in the coherent exciton dynamics in fmo. J. Phys. B, 45(15):154009, 2012.
- [36] M. Mohseni, P. Rebentrost, S. Lloyd, and A. Aspuru-Guzik. Environment-assisted quantum walks in photosynthetic energy transfer. J. Chem. Phys., 129:174106, 2008.
- [37] J. Adolphs and T. Renger. How proteins trigger excitation energy transfer in the fmo complex of green sulfur

- bacteria. Biophysical Journal, 91(8):2778, 2006.
- [38] Luis E Herrera Rodríguez and Alexei A. Kananenka. Convolutional neural networks for long time dissipative quantum dynamics. J. Phys. Chem. Lett., pages 2476–2483, 2020.